Chapter 1
Introduction: Ultra-Fast Response of Ultra-Thin Materials on Solid Surfaces

Ken-ichi Shudo

1.1 Introduction

1.1.1 Photoabsorption

"Something that makes things visible"
This is a dictionary definition of *light*. Originally a broad and ill-defined idea, in the modern parlance *light* usually refers to light that is visible (Vis) to the human eye, with a wavelength in the range of approximately 400–750 nm. Since light is understood as the propagation of *any* electromagnetic radiation, visible or otherwise, our concept of light has ultimately expanded to encompass a very wide range of wavelengths, from Ångströms to millimeters. These days, electromagnetic waves outside this range can also be referred to merely as *light*. We can now readily produce light spanning the entire spectrum, from the shortest wavelength light, called X-rays, to the longest, referred to as infrared (IR). Roughly speaking, light in the former of these wavelength ranges is usually considered to consist of particles with momenta $p = h\nu/c$, where h is Plank's constant, ν is the frequency, and c the speed of light, because scattering is most easily described in terms of momentum. The wavelengths ($\lambda = c/\nu$) of Vis and IR light may be vastly greater than the object to be observed if the object is very small, such as a nanometer-scale molecule. In such cases, the light interacts with charged particles in the object—protons in the nuclei and electrons—as a homogenous electric (and sometimes magnetic) field. Light in the Vis to ultraviolet (UV) range is often produced by electronic transitions, while IR is chiefly associated with spring-and-ball-like vibrations of molecules and lattice vibrations in crystals. Across the spectrum, light follows the wave-particle duality relation, $p = h/\lambda$, and the law of conservation of momentum holds for scattering between the object and

K. Shudo (✉)
Faculty of Engineering, Yokohama National University, Tokiwadai 79-5, 240-8501
Hodogaya-ku Yokohama, Japan
e-mail: ken1@ynu.ac.jp

K. Shudo et al. (eds.), *Frontiers in Optical Methods*,
Springer Series in Optical Sciences 180, DOI: 10.1007/978-3-642-40594-5_1,

the light. Developments in the techniques of light generation and detection allow a very wide variety of wavelengths to be utilized. The reader's interests need not be limited to the light itself, but may include the control and modulation of light and related phenomena.

In a material, electric and magnetic fields ($\boldsymbol{D}$ and $\boldsymbol{B}$, respectively) are induced by finite densities of electric and magnetic polarization ($\boldsymbol{P}$ and $\boldsymbol{P}_m$, respectively), in a medium under external electric and magnetic fields ($\boldsymbol{E}$ and $\boldsymbol{H}$). The following relations define these quantities:

$$\boldsymbol{D} \equiv \epsilon \boldsymbol{E} = \epsilon_0 \boldsymbol{E} + \boldsymbol{P} \tag{1.1}$$

$$\boldsymbol{B} \equiv \mu \boldsymbol{H} = \mu_0 \boldsymbol{H} + \boldsymbol{P}_m \tag{1.2}$$

where ϵ is the dielectricity and μ the magnetic permeability of the material. Note the suffix zero denotes the vacuum value, implying $\boldsymbol{P} = \boldsymbol{0}$ and $\boldsymbol{P}_m = \boldsymbol{0}$. The electric polarization plays an important role in the photoabsorption and reflection of light by the material.

All these physical quantities are governed by Maxwell's equations:

$$\nabla \cdot \boldsymbol{D} = \rho \tag{1.3}$$

$$\nabla \cdot \boldsymbol{B} = 0 \tag{1.4}$$

$$\nabla \times \boldsymbol{E} = -\frac{\partial}{\partial t} \boldsymbol{B} \tag{1.5}$$

$$\nabla \times \boldsymbol{H} = \frac{\partial}{\partial t} \boldsymbol{D} - \boldsymbol{J} \tag{1.6}$$

which are mediated by the electric charge density ρ and the electric current density $\boldsymbol{J}$. Two wave equations, derived from (1.3) through (1.6),

$$\nabla^2 \boldsymbol{E} = c' \frac{\partial^2}{\partial t^2} \boldsymbol{E} \tag{1.7}$$

$$\nabla^2 \boldsymbol{B} = c' \frac{\partial^2}{\partial t^2} \boldsymbol{B} \tag{1.8}$$

give simple independent solutions of the electric and magnetic fields at the point $\boldsymbol{r}$ and time t

$$\boldsymbol{E} \equiv \boldsymbol{E}(\boldsymbol{r}, t) = \boldsymbol{E}_0 e^{i(\boldsymbol{k}\cdot\boldsymbol{r} - \omega t)} \tag{1.9}$$

$$\boldsymbol{B} \equiv \boldsymbol{B}(\boldsymbol{r}, t) = \boldsymbol{B}_0 e^{i(\boldsymbol{k}\cdot\boldsymbol{r} - \omega t)}. \tag{1.10}$$

These fields propagate with velocity $c' = c/n$ through a material with refractive index $n = \sqrt{\frac{\epsilon\mu}{\epsilon_0\mu_0}}$ (note that the velocity of light in a vacuum is $c = \sqrt{\frac{1}{\epsilon_0\mu_0}}$). The optical responses of materials — how waves of light propagate through it — are formulated in terms of the modulation of the above wave equations. The assumptions that the materials are non-magnetic ($\mu \simeq \mu_0$) and electrically neutral ($\rho = 0$) are sufficient to discuss the following issues.

In a material medium, light is absorbed. This can be expressed mathematically as an expansion of the definition of the refractive index . Rather than using a purely real number n to describe the refractive index, the complex number $\tilde{n} = n + i\kappa$ can be introduced, where n and κ are real ($i^2 = -1$). Consequently, the wavevector $\tilde{k} = k' + ik''$, and the dielectricity $\tilde{\epsilon} = \epsilon_1 + i\epsilon_2$ of the corresponding wave equations are complex. The propagating wave at depth z can then be derived from (1.9) as

$$\boldsymbol{E} = \boldsymbol{E}_0 e^{i\omega(\frac{n}{c}z - t) - \frac{\omega\kappa}{c}z} \tag{1.11}$$

and the intensity (density of energy of the electric field) is given by

$$I = I(z) = \frac{\epsilon}{2}|\boldsymbol{E}|^2 = I_0 e^{-\alpha z} \tag{1.12}$$

where $\alpha = 2\omega\kappa/c$ is called the absorption coefficient of the material with extinction coefficient κ. Thus, one irradiates a material of thickness d with light of wavelength λ, and the intensity of the light that emerges from the other side of the material is reduced by the exponential factor $e^{-\alpha d}$. Equivalently, α can be determined from the intensity I of light that passes through the material. Determining the wavelength (or energy) dependence of α is the most classic form of *spectroscopy*. This is directly related to the dielectricity, which determines transmission and reflection. However, these can be modulated by irradiation with high intensity light. This modulation, chiefly due to the generation of excited electronic states and crystal lattice vibrations, maintains a oscillatory phase. This type of modulation, referred to as *coherent*, is emphasized here, because most optical techniques utilize the interference of light. Contemporary applications of coherence are addressed in the following Chapters. The macroscopic quantities described above can be explained in terms of photon-electron and electron-lattice interactions. Thus, electronic and lattice behavior can be analyzed with appropriate light sources. As the size of the material will be smaller than the wavelength of the irradiated light in most cases, we must deal with these quantities within the framework of quantum mechanics of object material systems.

Consider the Schrödinger equation, with Hamiltonian $\hat{H}$, where we define $\hat{H}_0$ as the electronic Hamiltonian without electromagnetic fields due to the incident light,

$$i\hbar\frac{\partial}{\partial t}\psi = \hat{H}\psi. \tag{1.13}$$

This can be rewritten as a secular equation $\hat{H}\psi = \mathcal{E}\psi$ in the case of stationary states. This has solutions indexed by their state j, represented by a wavefunction $\psi = \phi_j(\boldsymbol{r})$ with eigenvalue $\mathcal{E}_j$, corresponding to the energy of the electron. If one does not consider thermal effects at high temperatures, the highest energy states which are occupied by electrons, called the Fermi level E_F, is simply obtained from Pauli's exclusion principle. When the system is irradiated with light, the photoabsorption is described in terms of the probability of an electron in a ground state (ϕ_g with energy below the Fermi level) to make a transition into an excited state (ϕ_x above

the Fermi level). To deal simply with the electromagnetic field of light, we use a simple electric-dipole approximation. Because magnetic fields do not do work on the electrons, they are not considered here, as spin and angular momenta cancel macroscopically in most non-magnetic ($\boldsymbol{P}_m = \boldsymbol{0}$, or $\mu \simeq \mu_0$) materials. Including the electric field $\boldsymbol{E}$ as a perturbation, the Hamiltonian becomes

$$\hat{H} = \hat{H}_0 + \hat{H}' \tag{1.14}$$

with the electric potential energy of electrons j at point $\boldsymbol{r}_j$ being given by

$$\hat{H}' = \sum_j -\boldsymbol{E}(\boldsymbol{r}) \cdot (-e)\boldsymbol{r}_j, \tag{1.15}$$

where $\boldsymbol{E}$ is the externally applied light. Note that $\boldsymbol{M} = \sum_j (-e)\boldsymbol{r}_j$ is the electric dipole moment of the system with each elemental charge $-e$. The wavelength of ultraviolet (UV) light with photon energy up to $\sim$10 eV is of the order of 100 nm. Wavelengths in the region of Vis to UV are much larger than the atomic scale, and the external field can be well described as a spatially uniform, but time-dependent, field.

Expanding the wavefunction in Schrödinger's equation in terms of the sates ϕ_j and their (time dependent) amplitudes $b_j(t)$, such that $\psi = \sum_j b_j(t)\phi_j$, the time evolution of the amplitudes are expressed as

$$i\hbar \frac{\partial}{\partial t} b_j(t) = \sum_l b_l(t) H'_{j,l} e^{i\omega_{j,l}t}, \tag{1.16}$$

with matrix elements

$$H'_{j,l} = \left\langle \phi_l | \hat{H}' | \phi_j \right\rangle. \tag{1.17}$$

An initial condition may be that the initial state of a perturbed wave function is $\psi = \phi_g$ at $t = 0$. If the basis set of wavefunctions ϕ_j is normalized, the coefficient

$$\frac{\partial}{\partial t} b_j(t) = \frac{i\boldsymbol{M} \cdot \boldsymbol{E}_0}{\hbar} \cos\omega_{j,g} t \, e^{i\omega t} \tag{1.18}$$

is easily obtained, where a difference of the eigenfrequencies $\omega_{j,g} = \frac{\mathcal{E}_j - \mathcal{E}_g}{\hbar}$ is used. An extinction term is added for a realistic description of the finite lifetime that the excited state generally has, and it becomes

$$\frac{\partial}{\partial t} b_j(t) = \frac{i\boldsymbol{M} \cdot \boldsymbol{E}_0}{\hbar} \cos\omega_{j,l} t \, e^{i\omega t} - \frac{\Gamma}{2} b_j(t) \tag{1.19}$$

which makes the probability $|b_j(t)|^2$ of a component j decay as $\propto e^{-\Gamma t}$. Finally, the focused component of the excited state x is described in terms of the coefficient

$$b_x(t) = \frac{i\boldsymbol{M}\cdot\boldsymbol{E}_0}{2\hbar}\left\{\frac{e^{i(\omega+\omega_{x,g})t}}{\omega+\omega_{x,g}-i\frac{\Gamma}{2}}+\frac{e^{i(\omega-\omega_{x,g})t}}{\omega-\omega_{x,g}-i\frac{\Gamma}{2}}\right\}. \tag{1.20}$$

In isotropic media, the averaged product of $|\boldsymbol{M}\cdot\boldsymbol{E_0}|^2$ over all directions can be replaced by $\frac{1}{3}|\boldsymbol{M}|^2|\boldsymbol{E_0}|^2$). As the intensity of excited state formation is $|b_x|^2$, from (1.20), the averaged transition (photoabsorption) probability (frequency per unit time) in the medium due to the applied light of intensity I, is given by

$$B = \lim_{t\to\infty}\frac{|b_x(t)|^2}{t\,I} = \frac{\pi M^2}{3\epsilon_0\hbar^2}, \tag{1.21}$$

which is referred to as Einstein's B-parameter. Essentially, this is the origin of what is called a spectrum: B plotted against energy (or frequency). This classic picture is still remarkably eloquent, being able to deal with the propagation of electromagnetic fields through materials. This dipole model is often applied to molecular systems, as an isolated molecule is spatially limited to the scale of nanometers. Eigenvalues of a molecule are discrete, being separated by an energy gap of the order of an eV, and corresponding electronic transitions resonantly occur in the Vis to near-UV region. Although the reason for the decay is yet to be clarified, spontaneous and artificial relaxation of excited electrons is now able to be observed, owing to the advent of ultrafast lasers with the ability to achieve femtosecond pulse durations. A contemporary discussion of topics in quantitative experiments is given in the ensuing chapters.

1.1.2 Electronic Bands

In solids, the scale of the system can be larger than the wavelength of Vis to near-UV light. To overcome this, infinite periodicity is assumed in order to solve the wave equation of electrons. A solution of the Schrödinger equation in an infinitely periodic potential is called a Bloch state, which forms electronic bands. Electrons with a momentum $\boldsymbol{p}$ are identified by a wave vector $\boldsymbol{k} = \boldsymbol{p}/\hbar$ shown in Fig. 1.1a. As electronic states in different Brillouin zones are identical, the states are identified with a value of $\boldsymbol{k}$ in the first Brillouin zone. Photoabsorption is an electronic transition between two bands. Figure 1.1(b) shows electronic bands, for example, of a Si crystal whose structure is face-centered cubic (f.c.c). As the momentum of a photon is negligibly small compared with the momentum of Bloch electrons, the momentum of an electron can be considered to be constant during an electron-photon collision. Electronic transitions by photoabsorption process are thus shown as vertical arrows, as shown in Fig. 1.1b. In these cases, the dipole approximation takes another form. The perturbed Hamiltonian of a charged particle (with an electronic charge q), is [1],

$$\hat{H} = \frac{1}{2m}\left(\hat{\boldsymbol{p}} - q\boldsymbol{A}\right)^2 + \hat{V} \tag{1.22}$$

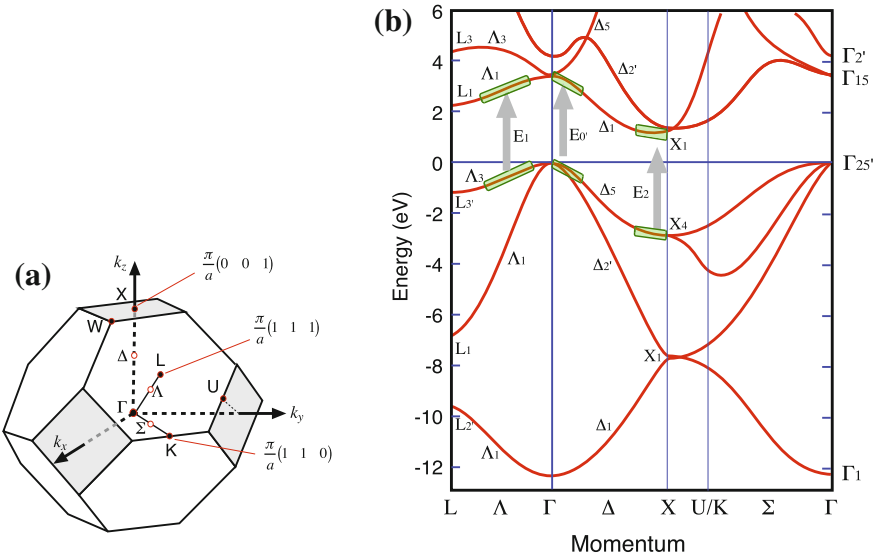

Fig. 1.1 **a** Electronic momenta in reciprocal space $\boldsymbol{k} = (k_x, k_y, k_z)$. The polygon defines the first Brillouin zone of a f.c.c. lattice with lattice constant a. Symbols of high symmetry points, after [2], are marked at various points. **b** Band structure of a silicon crystal along the momentum $\boldsymbol{p} = \hbar\boldsymbol{k}$, following a path between symmetry points in the Brillouin zone. The vertical axis is the electronic band energy, defined to be zero with respect to the valence band maximum. Data is taken from [3]. Vertical arrows indicate typical photo-transitions

in which the vector potential is $\boldsymbol{A}$, the momentum operator $\hat{\boldsymbol{p}} = \frac{\hbar}{i}\nabla$, and the potential due to electrons and nucleus is $\hat{V}$. This form of the interaction is called the minimal interaction representation, or minimal coupling, of the electromagnetic field. Equations (1.14) and (1.15) describes one of the converted forms of this formula (See Appendix A).

Some people prefer (1.22) because this form of Hamiltonian explicitly contains both electric and magnetic fields, and also because this formula is in a relativistically invariant form [4]. From the point of view of optical transitions, this is particularly easy to use

$$\hat{H} = \hat{H}_0 + \hat{H}' \tag{1.23}$$

$$\hat{H}_0 = -\frac{\hbar^2}{2m}\nabla^2 + \hat{V} \tag{1.24}$$

$$\hat{H}' = \frac{q}{2m}\left(\boldsymbol{A}\cdot\hat{\boldsymbol{p}} + \hat{\boldsymbol{p}}\cdot\boldsymbol{A}\right) \tag{1.25}$$

$$\simeq -\frac{e}{m}\left(\boldsymbol{A}\cdot\hat{\boldsymbol{p}}\right), \tag{1.26}$$

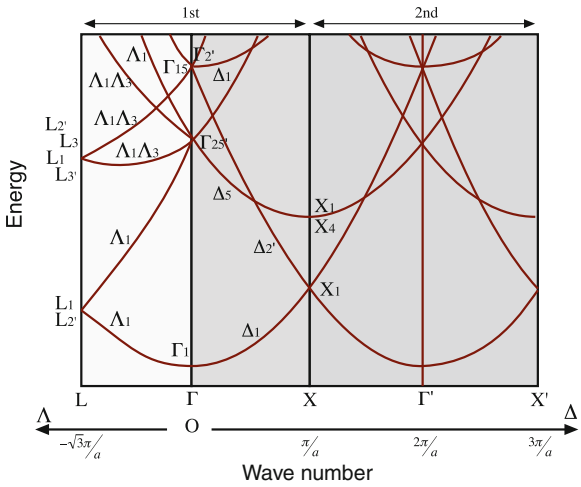

Fig. 1.2 The band structure of a free electron in a f.c.c. crystal, as a function of wave vector $\boldsymbol{k}$, in the directions of Λ and Δ. In the first Brillouin zone, they are the same directions as in Fig. 1.1. Along the Δ direction (*gray* areas), the adjacent second zone is also drawn, to make the parabolic nature of the dispersion clear

where $q = -e$ and the Coulomb gauge ($\nabla \cdot \boldsymbol{A} = 0$) has been used. The long wavelength limit ($\boldsymbol{A} \cdot \nabla = \nabla \cdot \boldsymbol{A}$) of the last approximation is taken. A quantity $|\boldsymbol{A}|^2$ is generally omitted as it is much smaller than $\boldsymbol{A} \cdot \hat{\boldsymbol{p}} + \hat{\boldsymbol{p}} \cdot \boldsymbol{A}$. The term $|\boldsymbol{A}|^2$ gives the energy density of the electromagnetic field of the irradiated light, and is taken to be a constant value if the photoabsorption is weak. When the incident light is very strong, or the medium material has particularly strong photo-absorption, this term should be considered because second order processes may occur. One sets $\boldsymbol{k}$ parallel to the direction of propagation of the electromagnetic field, then the Coulomb gauge enforces that the transverse wave ($\boldsymbol{A}$ perpendicular to the propagation direction) is

$$\boldsymbol{A}(\boldsymbol{r}, t) = \boldsymbol{A}_0 e^{i(\boldsymbol{k}\cdot\boldsymbol{r} - \omega t)} \tag{1.27}$$

$$\nabla \cdot \boldsymbol{A} = \boldsymbol{A}_0 \cdot \boldsymbol{k} e^{i(\boldsymbol{k}\cdot\boldsymbol{r} - \omega t)} = 0 \tag{1.28}$$

for all $(\boldsymbol{r}, t)$. Thus,

$$\boldsymbol{E} = -\frac{\partial}{\partial t}\boldsymbol{A}(\boldsymbol{r}, t) = i\omega \boldsymbol{A}_0 e^{i(\boldsymbol{k}\cdot\boldsymbol{r} - \omega t)} \tag{1.29}$$

$$\boldsymbol{B} = \nabla \times \boldsymbol{A} \qquad = i\boldsymbol{k} \times \boldsymbol{A}_0 e^{i(\boldsymbol{k}\cdot\boldsymbol{r} - \omega t)}. \tag{1.30}$$

This is a standard expression for a light wave in the semiclassical treatment of radiation [5].

The result from reciprocal (i.e., $\boldsymbol{k}$-) space with (1.26) and that from real ($\boldsymbol{r}$-represented) space in (1.15) must be the same (See Appendix B). To analyze interband transitions, it is most easy to handle the transition perturbation in $\boldsymbol{k}$-space than in $\boldsymbol{r}$-space, because the dispersion is plotted as a function of a good quantum number (momentum or wavenumber). A parabolic band structure of free electrons (described in terms of plane waves) in a f.c.c. lattice is shown in Fig. 1.2. This is very similar

to that of actual Si bands in Fig. 1.1. This indicates that the real band may be well approximated by plane wave states. A slight difference between the two, and one which is very important to us here, is the band gap near E_F. An actual wavefunction ψ consists of a plane wave, with wavenumber $\boldsymbol{k}$, as well as higher order components with the wave number shifted by $\boldsymbol{G}$; see duplicity between regions $\Gamma - X$ and $\Gamma' - X'$, for example. The shift $\boldsymbol{G}$ is a reciprocal lattice vector, defined as $\frac{2\pi}{a}(n_x, n_y, n_z)$ with $n_{x,y,z} = \pm 1, \pm 2, \ldots$. The resultant wavefunction of the electron is

$$\phi_{\boldsymbol{k}}(\boldsymbol{r}) = \sum_{n_x,n_y,n_z} C_{n_x,n_y,n_z}(\boldsymbol{k}) e^{i(\boldsymbol{k}-\boldsymbol{G})\cdot\boldsymbol{r}}, \tag{1.31}$$

where $C_{0,0,0} \simeq 1$. Note that a set of integers (n_x, n_y, n_z) describes the three-dimensional Brillouin zone. These higher order contributions, which deviate from the free electron state, are generated by the perturbing potential V, which originate from the underlying lattice and those electrons other than the nearly free electron being described. After performing a Fourier expansion of the potential, given by

$$V(\boldsymbol{r}) = \sum_{n_x,n_y,n_z} V_{n_x,n_y,n_z} e^{i\boldsymbol{G}\cdot\boldsymbol{r}}, \tag{1.32}$$

a potential component V_{n_x,n_y,n_z} primarily affects the coefficient C_{n_x,n_y,n_z} of the perturbed wavefunction [6]. A realistic band, as shown in Fig. 1.1, can be obtained with only a few potential components [7] in a simple and highly symmetric crystal structure such as silicon. Thus, the transition matrix element of the perturbation term, (1.26), is

$$\left\langle \phi_j | \hat{H} | \phi_g \right\rangle = -\frac{e}{m} \left\langle \phi_j | \boldsymbol{A} \cdot \hat{\boldsymbol{p}} | \phi_g \right\rangle \tag{1.33}$$

$$= -\frac{e}{m} \boldsymbol{A} \cdot \sum_{n_x,n_y,n_z \neq 0} \left\langle \phi_j | \hat{\boldsymbol{p}} | \phi_g \right\rangle \tag{1.34}$$

$$\simeq -\frac{e\hbar}{m} \boldsymbol{A} \cdot \sum_{\text{few } n_x,n_y,n_z} (\boldsymbol{k} + \boldsymbol{G}) \left\langle \phi_j | \phi_g \right\rangle. \tag{1.35}$$

Remember that both ϕ_j and ϕ_g have the same wave vector $\boldsymbol{k}$, because momentum conservation restricts the transitions vertical as the arrows in Fig. 1.1. Sets of coefficients $\left\{C_{n_x,n_y,n_z}\right\}$ in (1.35), differ slightly from (1.31), determine the wavefunctions. Therefore, the term $\left\langle \phi_j | \phi_g \right\rangle$ can easily be obtained, and is given by

$$\left\langle e^{i(\frac{p}{\hbar} - \boldsymbol{G})} | e^{i(\frac{p}{\hbar} - \boldsymbol{G})} \right\rangle = \frac{1}{2\pi} \sum_{\text{the few } n_x,n_y,n_z} C^*_{n_x,n_y,n_z}(j) C_{n_x,n_y,n_z}(g) \tag{1.36}$$

Thus, the transition probability can be obtained and it should be proportional to the imaginary part of the dielectricity (ϵ_2). The reflectivity is also calculated from ϵ_2,

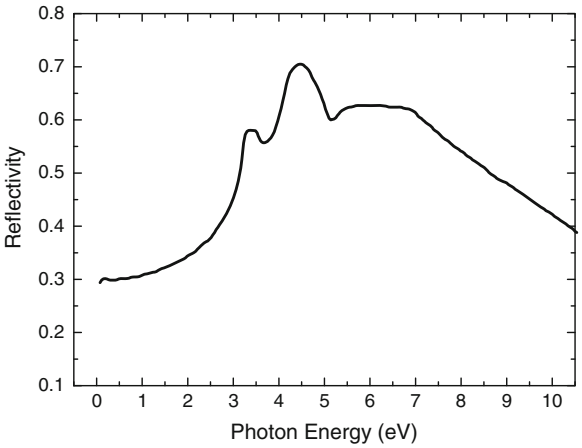

Fig. 1.3 Reflectivity spectrum of a crystalline Si surface. Data is taken from [8]

and agrees well with experiments [10, 8] (see the next section). An experimentally observed reflectivity of Si is shown in Fig. 1.3. There are peaks in the reflectivity at approximately 3.2 and 4.3 eV. The lower peak has two components, E_0 and E_1, while the higher peak contains a single component, denoted E_2 [11]. Corresponding electronic transitions are marked as arrows in Fig. 1.1, which connect two nearly parallel bands [12]. The shape of the band, and the peaks around E_1 and E_2, are common to materials in the zinc-blend family [3]. In these regions, photoabsorption occurs with high probability [8].

1.2 Surface Systems

As synchrotron radiation (SR) can be utilized these days, we are able to measure the precise optical responses in the UV to X-ray region of the spectrum. With the light in these region, photoemission spectroscopy is available to obtain the density of state (DOS) [13]. Generally, in interpreting photoemission spectra, we must consider the DOS of the final state as well as the initial state [14]. With the tunable light source (i.e., SR, laser, etc.), we can choose the wavelength of the irradiated light to reveal the DOS. In the experimental measurements of optical responses and electronic states of materials, features specific to surface system should be considered generally as any probe or signal have to pass the interface/surface of the medium inevitably. On the other hand, electronic states can now be easily determined via numerical calculations within a density functional theory (DFT) scheme, and using pseudopotentials is effective with a generalized gradient approximation (GGA) so far as isolated or inner-core electrons can be replaced with the potentials [15, 16]. This method has been successfully applied to semiconductors [17], as well as transition and nobel

metal surfaces [18]. To obtain the density of states of a Si crystal, as shown in Fig. 1.4a, the reciprocal space was divided into an $8 \times 8 \times 8$ mesh, for example. The calculated spectra reproduce quite well the experimentally obtained spectrum for energies below the Fermi energy, E_F (Fig. 1.4c). However, there is a shoulder in the actual experimental data of clean Si. This is attributed to surface states, originating from the dangling bonds (unpaired electrons at the surface, pointing out towards the vacuum) [19]. To represent the surface of a system having infinite periodicity, we can employ a slab-like geometry (Fig. 1.5). A DOS spectrum of the slab calculated (with a $6 \times 6 \times 1$ $\boldsymbol{k}$-space mesh) is shown in Fig. 1.4b, and surface states below and above E_F are observed (indicated by arrows in the figure). Note that even a sparse $\boldsymbol{k}$-space mesh is sufficient to observe the surface states [20]. The escape depth of electrons (mean-free path without scattering) has a minimum value of around $\simeq$10 Å when the electron energy is a few tens of eVs [21, 22]. The intensity of the calculated surface state response is consistently similar to that observed in the experimental spectra.

When a Si crystal is compressed or expanded, the electronic states change. In the chapter on the topic of high-pressures, a description is given of how the optical response of compressed materials is measured as temperature is varied. In Fig. 1.6, the calculated electronic states of a crystal are shown, where the lattice size of the crystal is changed isotropically. The total energy of a unit cell in the lattice, Fig. 1.6a, shows a parabolic well, which corresponds to the harmonic oscillator-like lateral breathing mode. This compression/expansion changes the electronic structure slightly, as shown in Fig. 1.6b plotted in terms of DOS. A shoulder at $E_F - 0.7$ and $E_F + 0.5$ eV

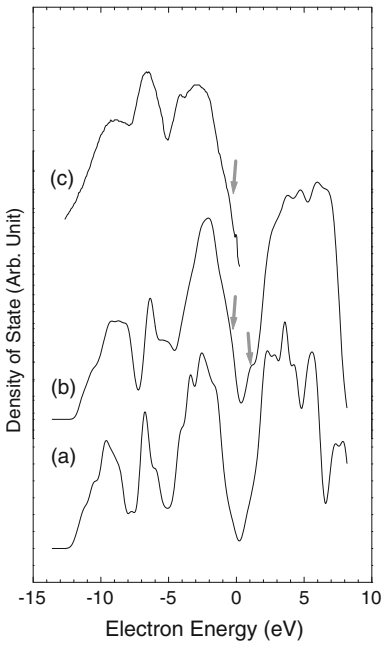

Fig. 1.4 The calculated density of states (DOS) with respect to valence band maximum of a silicon crystal. *a* Three-dimensional crystal with diamond lattice periodicity, representing a perfect bulk. *b* Two-dimensional structure of 6 layers of Si with a surface of Si dimers. The other surface was terminated with hydrogen. Surface states, which originate from dangling bonds at the dimers, appear as a shoulders in the DOS. *c* Photoemission spectroscopy using photons with energy $h\nu = 25$ eV. Data is taken from [9]

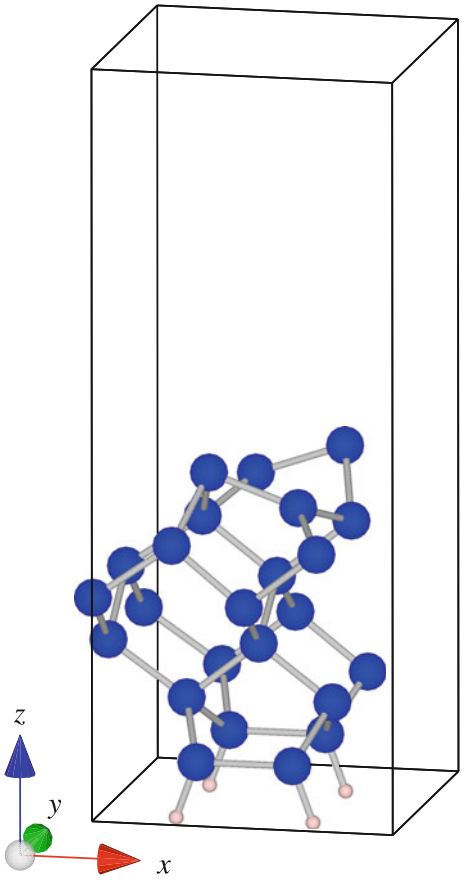

Fig. 1.5 An example of a slab, representing a surface. The structure is a p(2 × 2) structure of the Si(001) surface, containing two Si dimers buckled in different directions (toward $+x$ and $-x$) [19]. To terminate the dangling bond on the other side, extra hydrogen atoms are added (bottom of the slab)

shifts slightly due to this deformation. The bulk-derived state at $E_F \pm 1.5$ eV on the other hand, changes considerably, the shifts in the large peaks between -2.4 to -2.0 eV and between $+2.1$ and ~ 3 eV are particularly noteworthy. These correspond to the shift of the E_1 and E_2 peaks [12]. Thus, the transitions near E_0, E_1, and E_2 are all very sensitive to expansion (or other distortions) of the lattice. The reflection rate of photons with energy of a few eV changes when a phonon causes the lattice size to vibrate. With ultrafast pulsed lasers, real-time oscillations in the reflectance due to the compression/expansion of the lattice can be measured [23]. In the following chapters, such ultrafast measurements are introduced. On the other hand, it is very difficult to detect the surface states as compared with the bulk. However, the change of the surface states can be detected when the reflectance is precisely measured. In the next section, the particular case of the sensitivity of the reflectivity to the surface states is explained. Experimental results, by means of an optical modulation method, are addressed in another Chapter, and are also described in detail.

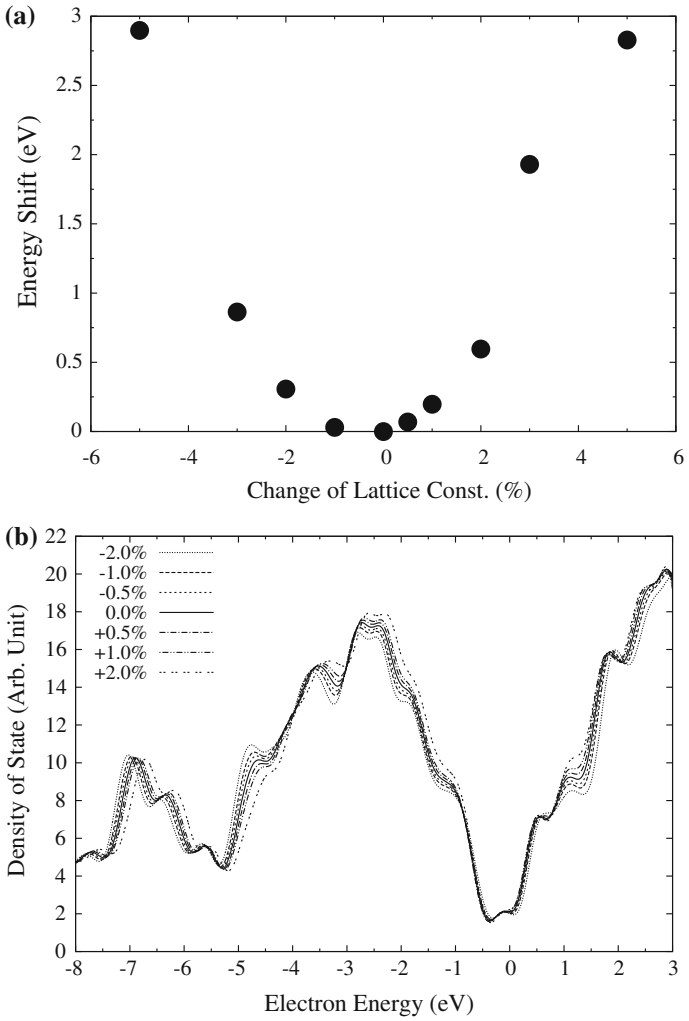

Fig. 1.6 **a** Calculated values of the relative energy per unit cell and **b** the density of states with respect to the Fermi level E_F of the slab model in Fig. 1.5 when the lattice constant is varied

1.2.1 Surface Reflectance

The optical response in terms of reflectivity has been widely used to measure thin films. Ellipsometry has been often applied to determine the thickness of a film on a surface if the dielectric constants of the substrate- and the surface-materials are known [24]. In recent years, optical spectroscopic methods, such as surface differential reflectivity (SDR) and reflectance difference spectroscopy (RDS) (sometimes referred to reflectance asymmetry (RA)), have been developed as powerful

tools to investigate the electronic properties of semiconductor surfaces and interfaces, even at the atomic scale [25–27]. The principle advantage of these methods is their ability to observe processes on the surfaces nondestructively in real time, even in high-pressure reactive gasses. However, optical spectra alone are not sufficient to provide an understanding of the surface structures and the electronic states that determine the optical responses. Theoretical analysis of the surface electronic states is necessary to interpret the optical spectra in terms of surface structures.

To assign the optical spectra to surface states, we calculated the electronic states and optical transitions of the Si(111) surface using small clusters. Although the Si(001) surface is chiefly used in silicon devices, Si(111) is more frequently used in research at the atomic scale, because of the variety of reactions due to its reconstructed structure. Thus, we report here the calculated optical spectra of the Si(111)-7×7 dimer–adatom–stacking-fault (DAS) surface [28]. The adsorption process of chlorine at the Si(111) surface can be divided into two stages. First, a chlorine atom reacts with silicon at adatom (AD) sites to form monochloride, to terminate the dangling-bond (DB) [29, 30]. When the adsorption density becomes almost equal to that of the adatoms, di- and trichloride begin to form [31, 32]. When these polychlorides are produced, one of the three adatom back-bonds (ADBB) is broken. Then, a Cl atom is bonded to the adatom, leaving a rest-atom dangling-bond (RADB) [33, 34]. We have calculated SDR spectra $\Delta R/R$ of the mono- and dichloride Cl/Si(111) surfaces, and analyzed the electronic states associated with features in the spectra.

1.2.2 Calculation

While density functional theory (DFT) deals only with the ground states, time-dependent density functional theory (TD-DFT) can deal with excited states as well as the ground states [35]. TD-DFT calculations can be performed on relatively small computers, such as desktop workstations. The calculation of optical spectra using TD-DFT has been reported not only for molecules [36], but also for solids [37], and TD-DFT allows the precise evaluation of the excited states of molecules. Clusters which contain 13 silicon atoms are sufficient for the present purpose, because Ricca et al. used clusters of this size to calculate the Si-Cl frequency using DFT, and the calculated value was in good agreement with the experimental value [38]. Therefore, we deem that this method should also be applicable to silicon surfaces. We calculated the electronic states and the optical transitions with the widely used *ab initio* calculation program Gaussian 03/09 [39].

The compositions of the clusters used to represent the T_4 site of Si(111) are $Si_{21}H_{27}$ for the clean surface, and $Si_{21}H_{27}Cl$ and $Si_{21}H_{27}Cl_2$ for chlorine-adsorbed surfaces. The last two represent monochloride and dichloride generated from the adatom, respectively. The geometric structures of the clusters used for the calculation are shown in Fig. 1.7. In order to eliminate all the dangling-bonds except at the Si adatom, all silicon atoms except the adatom are terminated by hydrogen atoms. In the calculation of the photo-transition energy of the clusters, the hybrid TD-DFT

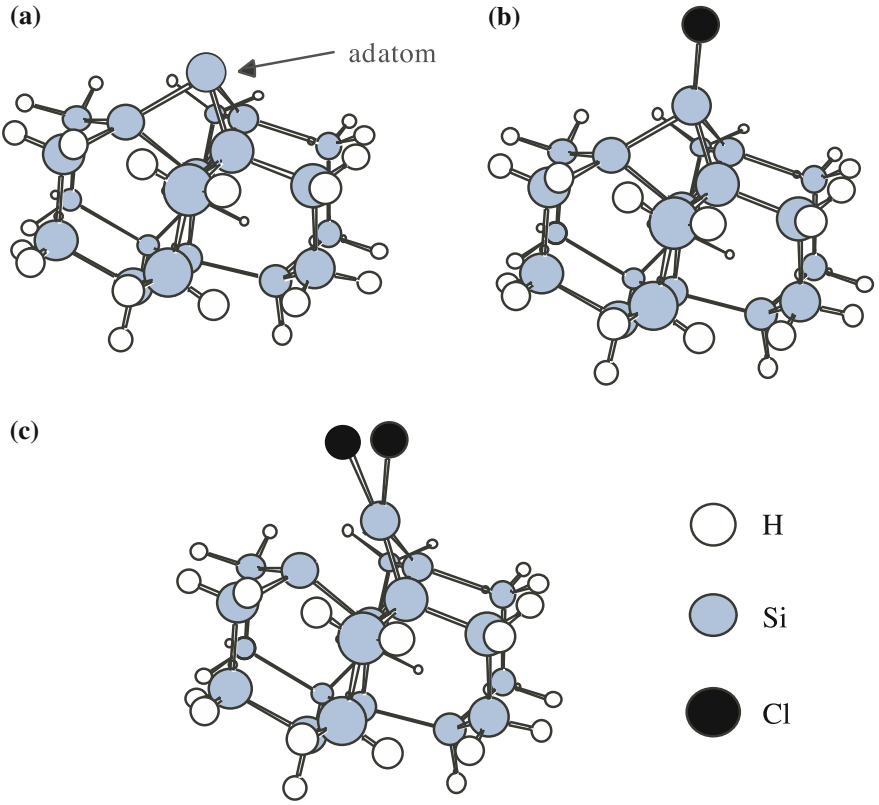

Fig. 1.7 Geometric structures of the clusters used to represent the Cl/Si(111) surface: **a** $Si_{21}H_{27}$, representing the clean surface; **b** $Si_{21}H_{27}Cl$ and **c** $Si_{21}H_{27}Cl_2$, representing chlorine-adsorbed surfaces

method was employed, because it gives the best agreement with experiment [40]. Furthermore, we selected the Becke 3-parameter hybrid functional with Lee, Yang, and Parr correlation (B3LYP), as the preferred tool [41, 42]. First, the geometry of the Si(111) clusters was energetically optimized at the 6-31G level. After the optimization, the calculations of electronic excitation were carried out with the 6-31G* basis set. The distribution of the wave-function relevant to the photo-transitions was examined with the visualization program Molden [43].

From the results for electronic excitations and oscillator strengths, optical transition probabilities were obtained. The oscillator strength f can be expressed in terms of transition probability μ as follows:

$$f_{ij} = \frac{2m\omega}{3e^2\hbar}|\mu_{ij}|^2 \tag{1.37}$$

in which i and j represent the initial and final states, respectively, and

$$\mu_{ij} = \frac{\langle \phi_j | \boldsymbol{e} \cdot \boldsymbol{p} | \phi_i \rangle}{|\boldsymbol{e}|}. \tag{1.38}$$

where $\boldsymbol{e}$ is the direction of the electric field.

The imaginary part, ϵ_2, of the dielectric function for frequency ω was obtained with the following expression [44, 45].

$$\epsilon_2(\omega) = \frac{4\pi^2 e^2}{m^2 \omega^2 A} \sum_{i,j} \delta[E_i - E_j - h\omega] \times |\mu_{ij}|^2, \tag{1.39}$$

where A is the volume of the cluster.

In the numerical calculation of (1.2), the δ-function is substituted by a normalized Gaussian function whose standard deviation is set to $0.1 \sim 0.15$ eV, because the photo-excitation has a band width of about this value in the bulk [46, 47] and at the surface [48]. The imaginary part is transformed into the real part through the Kramers-Kronig relation. Electronic transitions were calculated up to 6 eV, but this is not enough to calculate ϵ_2 and SDR spectra. To avoid this limit, ϵ_2 should be extrapolated to connect it to the imaginary part of the dielectric function in the bulk state [49]. Therefore, we multiplied the calculated ϵ_2 by a factor so that the imaginary part of the dielectric function in the bulk state is linked smoothly at energies greater than 3.1 eV for the clean surface and 4.9 eV for the Cl-adsorbed surface. Even if the factor is changed, the form of the SDR spectra does not qualitatively change. This factor corresponds to the cluster volume, A in (1.2). The index of refraction $n(\omega)$, the extinction coefficient $\kappa(\omega)$ and reflectance $R(\omega)$ can be derived using the complex dielectric function for the frequency ω. In the case of normal incidence, R can be expressed with Fresnel's formula.

Although s-polarized and p-polarized SDR spectra generally differ in intensity, the shapes of the spectra are very similar to each other in the case of Si(111) [26]. Consequently, we did not consider the polarization of incident light, and the calculation covered only normal incidence. By means of these procedures, an SDR spectrum $\Delta R/R$ can be calculated from the reflectances of the clean surface R_{clean} and the adsorbed surface $R_{\text{Cl-adsorbed}}$.

$$\frac{\Delta R}{R} = \frac{R_{\text{Cl-adsorbed}} - R_{\text{clean}}}{R_{\text{clean}}} \tag{1.40}$$

Next, we calculated the optical transitions of the cluster representing dichloride, shown in Fig. 1.7c, in which one of the ADBB is broken and terminated with a chlorine atom, and the rest-atom dangling-bond appears. The SDR spectrum for this back-bond breaking was calculated.

1.2.3 Example and Interpretation

Dangling-Bond termination

Calculated SDR spectra for monochloride formation during Cl-adsorption on Si(111) are shown in Fig. 1.8. The basis set effect between 6-31G and 6-31G* is negligible. Up to 3.2 eV, the spectrum computed with the 3-21G basis set resembles the other spectra. It is sufficient to analyze surface-to-surface transitions up to 3.2 eV, because electronic excitations of silicon above 3 eV are mainly contributed to by the bulk state. The positions of the peaks obtained with the 3-21G basis set are very close to those calculated with other basis sets, but the intensity is greater with 3-21G than with others. Although it is not yet clear why the intensity is sensitive to the basis set, the 3-21G basis set seems adequate to assign the spectral profile.

The experimental Cl/Si(111) SDR spectrum is shown in Fig. 1.9 [50]. The observed spectrum can be decomposed into two component spectra, S_A (a) and S_B. S_A corresponds to the negative peak at 1.55 eV in the calculated SDR spectra (b), similar to the assignment of the negative peak (c) for H/Si(111) to the calculated peak (d) at 1.4 eV [51]. Thus, the calculated feature at 1.55 eV (transition from the ADBB state to the antibonding ADDB state) is considered to be the origin of the main peak. The negative minimum in (b) and (d) at 2.1 $\sim$ 2.2 eV is due to the transition from an ADDB state to an antibonding ADBB state, although no peak was apparent experimentally. The calculated minimum at 2.8 eV, again not visible experimentally, is due to transitions from ADDB or ADBB to antibonding ADBB states and from bulk to antibonding ADBB states. As the energy becomes larger, bulk-to-bulk transitions become predominant, and above 2.8 eV, electronic transitions occur

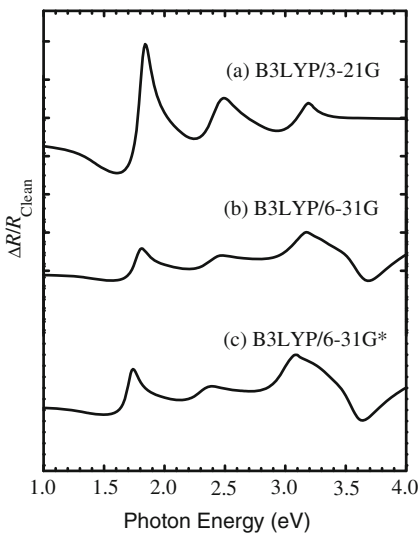

Fig. 1.8 Cl/Si(111) SDR spectra calculated with *a* B3LYP/3-21G,*b* B3LYP/6-31G, and *c* B3LYP/6-31G* basis sets

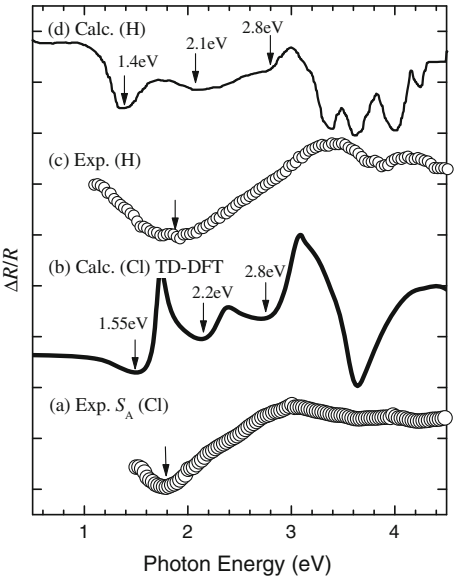

Fig. 1.9 SDR spectrum of S_A experimentally obtained for the monochloride Si(111) *a* and the spectrum obtained by calculation *b*. The experimental *c* and calculated *d* spectra of monohydride Si(111) [26] are plotted for comparison

mainly inside the bulk. Thus, the assignment of spectral features of the Cl/Si(111) surface is possible with this method. The features are quite similar to those obtained in the case of hydrogen.

Back-Bond breakage

We next focused on the process of ADBB breakage, namely the process of dichloride formation, with the cluster having with the newly emerged dangling-bond at the rest-atom. In the model, the dangling-bond at AD is terminated with the Cl atom, while a dangling-bond remains at RA. The inclination of adatom dichloride towards the RADB, set to the initial geometry shown in Fig. 1.7c, was almost removed after the energetic optimization, in accordance with a microscopic estimation of Cl density [52].

A spectrum was calculated through the same approach as in the case of dangling-bond termination, and is shown in Fig. 1.10 together with the observed spectrum, S_B. The ΔR is defined here as $\Delta R \equiv R_{\mathrm{SiCl_2}} - R_{\mathrm{SiCl}}$, as S_B represents the difference of reflectance between mono- and dichloride. The results for dihydride formation obtained by experiment (c) and by means of huge cluster calculations (d) for hydrogen adsorption [26] are also plotted.

All the spectra in Fig. 1.10 contain a negative peak at around 2.6 ∼3.0 eV. This peak can be assigned to the loss of the transition at AD, owing to the missing BB. This assignment turned out to be commonly applicable to ADBB breaking by halogen and hydrogen. Thus, the TD-DFT method with small clusters is capable of interpreting

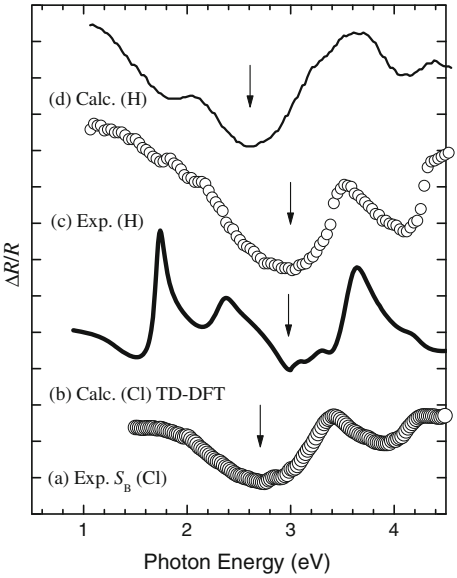

Fig. 1.10 **a** SDR spectrum of S_B experimentally obtained for the dichloride Si(111) and **b** the same spectrum obtained by a calculation. Experimental **c** and calculated **d** spectra for the dihydride [51] are also shown, for comparison

the SDR spectra for adsorption of elements with large electron affinity, such as chlorine. However, the spectrum (b) has some features below ∼2 eV. These may be caused by a perturbation of the remaining ADBB by the additionally adsorbed Cl atom, possibly through charge transfer from Cl to AD, as suggested by a previous calculation [53]. Although some transitions from/to the emerged DB at the rest-atom are from 2.6 eV and above, the effect of this kind of DB is still unclear. Further analysis will be required, however it is clear that the surface electronic transition is strongly affected by the surface electronic structure. Reflectance spectroscopy is dominated by the transition, and the surface structure, in terms of adsorbates and electronic states, can be elucidated with spectroscopic information.

1.3 Ultrafast Measurement

1.3.1 Monolayer Film of Organic Molecule

Among organic molecules, the thiol family is known to easily form a self-assembled monolayer (SAM) film with a bond at the sulfur site, even to noble metal surfaces. A benzentiol (BT) molecule contains the most fundamental aromatic functional that offers a variety of applications [54]. As molecular vibrations of such SAMs are fingerprints of adsorbed structures, we consider the dynamic motion of the molecules to elucidate molecule-substrate interactions in the ultrathin film. Ultrafast measurements of coherent molecular motion at the femtosecond time-scale are available with

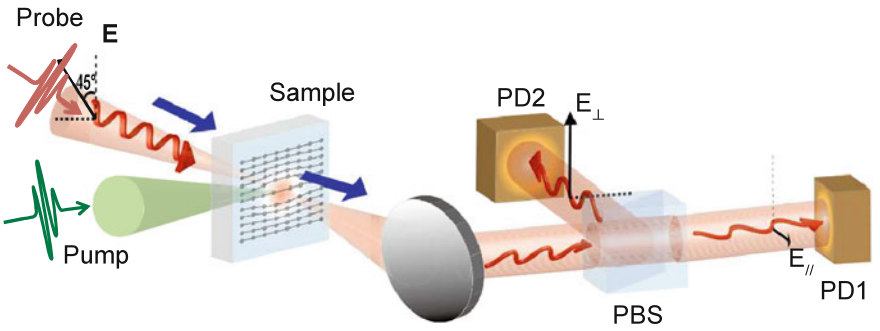

Fig. 1.11 Schematic illustration of the experimental setup for ultrafast transmission/absorption measurements

optical methods using ultrashort-pulsed laser systems. In this research, we measured the transient reflectance signal from a Au surface, on which the SAM of BT was adsorbed at the monolayer thickness. The resultant frequency domain spectra gave information on coherent motion of the adsorbed layer.

Strips of silicon (001) wafer were used as a substrate material. Prior to optical measurements the specimens were treated as follows: gold (Au) atoms were attached to the surface by sputter deposition to form Au films with thicknesses of a few Angstrom to several nm. The specimen was then soaked in an ethanol solution of BT (1 mM) for 24 hrs. On the Au surface, BT molecules were adsorbed at a monolayer thickness [55]. The surface morphology of Au was confirmed via atomic-force microscopy.

To obtain the ultrafast response, ultrashort pulses (7.5 fs) of a Ti:sapphire laser (800 nm) were used as a light source. For the liquid phase of the organic molecules, the transmission anisotropy was measured in real time by means of a pump-probe technique in electro-optical (EO) sampling configuration (Fig. 1.11). At the surface of the specimen, the optical response was measured in the reflectance configuration [57]. A pump beam was irradiated from the direction normal to the surface, and the beam was focused at the surface. A probe pulse delayed variably from the pump pulse was focused to the surface area where the pump was irradiated. The transmitted/reflected probe beam was divided into two polarized components orthogonal to each other. The difference of the intensities of the two components, measured with a pair of photodiodes, was detected electrically. This difference was taken as the sign of asymmetry in the optical reflectance due to surface deformation.

1.3.2 Experimental example

The transient signal of a BT monolayer film was plotted along the varied delay time as shown in Fig. 1.12. After an intense signal was observed initially (where 0 delay

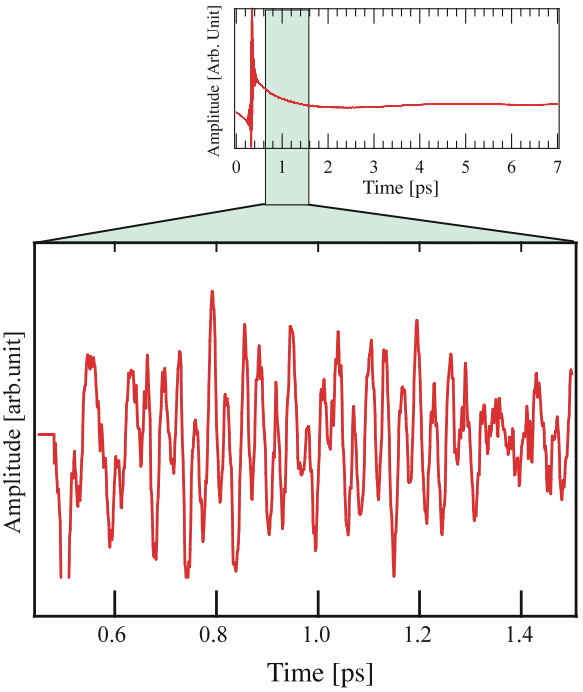

Fig. 1.12 Magnification of the real-time transient response, plotted after subtraction of a slow component. The upper panel is an observed transient response of the surface asymmetry in reflectance (EO sampling; see Text). The shadowed area in the upper panel corresponds to the main panel. Data taken from [56]

is at 0.37 ps), a slow decay was observed. After subtraction of the decay, a complex oscillatory signal remained (shown in the main panel). In the Fourier transformed spectra Fig. 1.13 from the residual signal, several peaks are found. In the figure, we also plotted peaks of vibrational components of liquid BT (> 98 % purity) obtained with conventional c.w.-Raman spectroscopy.

Most of the peaks in the Fourier spectra (gray in Fig. 1.13) correspond roughly to the vibrational peaks in the conventional spectra (black in Fig. 1.13). No peak due to the Si substrate was observed in the Fourier spectra, because we are able choose a polarization of the incident beam so as to excite the surface layer selectively, based on a selection rule associated with photoexcitation [23]. On the other hand, a peak originating from the crystalline Si (∼16 THz) appeared as the strongest signal in the C. W. -Raman data (not shown). Thus, we can selectively distinguish the coherent motion of the two-dimensional structure of the BT monolayer, as the ultrashort pulses excite the SAM film impulsively. There are some discrepancies in the peak positions between the SAM film and the liquid phase. These vibration shifts can be explained in terms of immobilization of the molecule at the Au surface [54]. We calculated electronic and vibrational eigenvalues with a first-principle method, and the vibronic

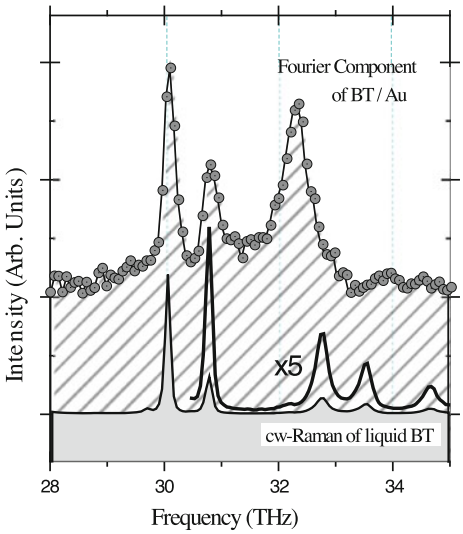

Fig. 1.13 Fourier components (hatched) of the subtracted signal (main panel in Fig. 1.12). Only a small range of the data, displaying typical peaks, is shown. In comparison, a conventional Raman spectra of liquid BT is shown (*gray*), which is magnified by a factor of five

modes of the BT adsorbed on the surface are in good agreement with the experimental results. The relative intensity of each mode varies when the thickness of Au deposition due to the sensitivity of Raman effect sensitive to the surface roughness [58]. This indicates the surface-enhanced Raman scattering (SERS) effect is active at the surface layer also in reflectance [57]. Morphology of the Au surface and alignment of the molecules seem to affect the ultrafast dynamics; the ultrafast pump-and-probe measurement enables us to discuss dynamic phenomena of real-time coherent motion in the monolayer thin films.

Using the pump-probe EO sampling technique, it is possible to selectively and sensitively measure the transient optical asymmetry originating from the vibration of organic molecules adsorbed on surfaces. To discuss the intermolecular, nonlinear, and low-dimensional lattice interactions in such molecular systems, real-time analysis gives new information [59] in terms of time-dependent intensity, phase, and beat frequency of each vibronic mode.

1.4 Summary

In this introductory chapter, the relation of the optical response of a material with its electronic states has been addressed. Next, the optical response of a surface system in the Vis to UV region was shown to be sensitive to an atomic-scale adsorbed material. The assignment of the electronic excitations for Cl/Si(111) was explained by means of calculations carried out in the TD-DFT regime, using small clusters. Finally, an ultrafast response of monolayer molecules adsorbed on a solid surface was discussed. This response was then related to the molecular vibronic modes, and

the information about the real-time oscillations enables us to elucidate the vibronic phase and amplitude. This in turn gives information on atomic/molecular motion, including photo-induced excitation and relaxation processes.

1.5 Acknowledgment

The author is grateful to Prof. Masanobu Uchiyama (Riken, The Institute for Chemical and Physical Research) and Mr. M. Mori and Ms. E. Senga (Information Processing Center, YNU) for computational support. The calculations were partly performed on the Riken Integrated Cluster-of-Clusters (Riken) and the Supercomputer Facility at the Institute for Solid State Physics (the University of Tokyo), under advice concerning TD-DFT by Prof. Kaoru Ohno (YNU) and Dr. Soh Ishii (YNU). The author also thanks Mr. Tatsuya Momose for his assistance in performing the calculations and plotting the results, and Mr. Koshiro Doi for his assistance in analysing and drawing the ultrafast measurement data.

Appendix: A Long-Wavelength Approximation

Whenever a gauge transformation with a function χ,

$$\boldsymbol{A} \mapsto \boldsymbol{A}' = \boldsymbol{A} + \nabla\chi \tag{A.1}$$

$$U \mapsto U' = U - \frac{\partial}{\partial t}\chi, \tag{A.2}$$

is applied to a vector and scalar electromagnetic potential, $\boldsymbol{A}$ and U, simultaneously, the resultant fields $\boldsymbol{B}' = \nabla \times \boldsymbol{A}'$ and $E' = -\nabla U'$ are unchanged, such that

$$\boldsymbol{B} = \nabla \times \boldsymbol{A} \tag{A.3}$$

$$\boldsymbol{E} = -\nabla U'. \tag{A.4}$$

To eliminate the magnetic field in (1.22), we take a function $\chi = -\boldsymbol{r} \cdot \boldsymbol{A}$. Then, in the case that the wavelength of the irradiating light is much larger than the size of the system, such as in the case of molecules (or crystalline domains where the electronic diffusion/drift is limited), the electric and magnetic fields can be considered to be constant. Then,

$$\boldsymbol{A}' = \boldsymbol{A} - \big((\boldsymbol{A}\cdot\nabla)\boldsymbol{r} + (\boldsymbol{r}\cdot\nabla)\boldsymbol{A} + \boldsymbol{A}\times(\nabla\times\boldsymbol{r}) + \boldsymbol{r}\times(\nabla\times\boldsymbol{A})\big) \tag{A.5}$$

$$\simeq 0, \tag{A.6}$$

$$U' = U + \left((\frac{\partial}{\partial t}\boldsymbol{r})\cdot\boldsymbol{A} + \boldsymbol{r}\cdot\frac{\partial}{\partial t}\boldsymbol{A}\right) \tag{A.7}$$

$$= U - \boldsymbol{r}\cdot\boldsymbol{E}, \tag{A.8}$$

where we note that $\boldsymbol{r}$ is independent of time, t. Finally, with $\boldsymbol{A}$ corresponding to the external light source from (A.3) and (1.5). $V = -eU$ being the electron-nucleus potential, the Hamiltonian (1.22), becomes the pair of equations, (1.14) and (1.15). This result is to be somewhat expected, because the magnetic field does no work on a charged particle unless the spin of the particle is considered from relativistic invariance. To analyse the magnetic effect of spin, the dipole approximation is not enough.

Appendix: B Minimal Interaction in r-Space

The uncertainty of quantum mechanical theory can be expressed as

$$\hat{p}_x x - x\hat{p}_x = \frac{\hbar}{i}. \tag{B.9}$$

Then,

$$\frac{1}{m}\frac{\hbar}{i}\hat{p}_x = \left(\hat{p}_x\frac{1}{2m}(x\hat{p}_x + \frac{\hbar}{i}) + Vx\right) - \left(\frac{1}{2m}(\hat{p}_x x - \frac{\hbar}{i})\hat{p}_x + xV\right) \tag{B.10}$$

$$= \left(\frac{1}{2m}\hat{p}_x(\hat{p}_x x) + Vx\right) - \left(\frac{1}{2m}(x\hat{p}_x)\hat{p}_x + xV\right) \tag{B.11}$$

$$= \left(\frac{1}{2m}\hat{p}_x^2 + V\right)x - x\left(\frac{1}{2m}\hat{p}_x^2 + V\right) \tag{B.12}$$

$$= \hat{H}x - x\hat{H}, \tag{B.13}$$

and the other components of $\boldsymbol{p}$ follow the same relation, giving

$$\frac{1}{m}\frac{\hbar}{i}\hat{\boldsymbol{p}} = \hat{H}\boldsymbol{r} - \boldsymbol{r}\hat{H}. \tag{B.14}$$

Assuming an homogeneous electromagnetic field, $\boldsymbol{A}$, the transition matrix element (1.17) in (1.16), using the perturbative term (1.26), becomes

$$\hat{H'}_{g,j} = \frac{e}{m}\langle\phi_j|\boldsymbol{A}\cdot\hat{\boldsymbol{p}}|\phi_g\rangle \tag{B.15}$$

$$= \frac{ie}{\hbar}\boldsymbol{A}\cdot\left\langle\phi_j|(\overleftarrow{H}\boldsymbol{r} - \boldsymbol{r}\overrightarrow{H})|\phi_g\right\rangle \tag{B.16}$$

$$= \frac{ie}{\hbar}\boldsymbol{A}\cdot\left\langle\phi_j|(\mathcal{E}_j\boldsymbol{r} - \boldsymbol{r}\mathcal{E}_g)|\phi_g\right\rangle \tag{B.17}$$

$$= ie\frac{\mathcal{E}_j - \mathcal{E}_g}{\hbar}\langle\phi_j|\boldsymbol{r}|\phi_g\rangle, \tag{B.18}$$

which leads to the same result as (1.18).

References

1. P.A.M. Dirac, *The Principles of Quantum Mechanics*, 4th edn. (Oxford University Press, Oxford, 1982)
2. J. Cornwell, *Group Theory and Eectronic Energy Bands in Solids* (John Wiley and Sons, New York, 1969)
3. J.R. Chelikowsky, M.L. Cohen, Phys. Rev. **B14**, 556–582 (1976)
4. J.D. Jackson, *Classical Electrodynamics*, 3rd edn. (John Wiley & Sons, New York, 1999)
5. Refer, for example, to Chapter 11 in it Quantum Mechanics, 3rd ed. by L. I. Sciff (Mc-Grawhill Inc., New York, 1955–1969).
6. M.L. Cohen, T.K. Bergstresser, Phys. Rev. **141**, 556 (1976)
7. E.O. Kane, Phys. Rev. **146**, 558 (1966)
8. H.R. Philipp, H. Ehrenreich, Phys. Rev. **129**, 1550–1560 (1963)
9. W.D. Grabman, D.E. Eastman, Phys. Rev. Lett. **29**, 1508–1512 (1972)
10. J.R. Chelikowski, M.L. Cohen, Phys. Rev. B **14**, 789 (1966)
11. R.R.L. Zucca, Y.R. Shen, Phys. Rev. B **1**, 2668 (1970)
12. M. Cardona, *Modulation Spectroscopy* (Academic Press, New York, 1969)
13. H. Ibach (ed.), Electron Spectroscopy for Surface Analysis (Topics in Current Physics) (Springer, Berlin, 1977 (Original ed.)).
14. W. Schattke, E.E. Krasovskii, R. Díez, P.M. Echenique, Phys. Rev. B **78**, 155314 (2008)
15. K. Ohno, K. Esfarjani, Y. Kawazoe, *Computational Materials Science: From Ab Initio to Monte Carlo Methods, Springer Series in Solid-State Sciences* (Springer, Berlin, 2000)
16. R.M. Martin, *Electronic Structure: Basic Theory and Practical Methods* (Cambridge University Press, Cambridge, 2008)
17. Y. Morikawa, Phys. Rev. B **63**, 033405 (2001)
18. T. Hayashi, Y. Morikawa, H. Nozoe, J. Chem. Phys. **114**, 7615 (2001)
19. A. Zangwill, *Physics at Surfaces* (Cambridge University Press, Cambridge, 1988)
20. A. Ramstad, G. Brocks, P.J. Kelly, Phys. Rev. B **51**, 14504–14523 (1995)
21. T.N. Rhodin, J.W. Gadzuk, Nature of the Surface Chemical Bond, ed. by T.N. Rhodin, G. Erti (North-Holland, Amsterdam, 1979), pp. 113–273.
22. D.R. Penn, Phys. Rev. B **13**, 5248–5254 (1976)
23. M. Hase, M. Kitajima, A.M. Constantinescu, H. Petek, Nature **426**, 51–54 (2003)
24. H. Fujiwara, *Spectroscopic Ellipsometry-Principles and Applications* (John Wiley & Sons, New York, 2007)
25. M. Palummo, O. Pulci, R. Del Sole, A. Marini, P. Hahn, W.G. Schmidt, F. Bechstedt, J. Phys.: Condens. Matter **16**, S4313 (2004)
26. C. Noguez, C. Beitia, W. Preyss, A.I. Shkrebtii, M. Roy, Y. Borensztein, R. Del Sole, Phys. Rev. Lett. **76**, 4923 (1996)

27. S. Ohno, T. Ochiai, M. Morimoto, T. Suzuki, K. Shudo, M. Tanaka, Jpn. J. Appl. Phys. **49**, 055702 (2009)
28. K. Takayanagi, Y. Tanoshiro, S. Takahashi, M. Takahashi, Surf. Sci. **164**, 367 (1985)
29. J.S. Villarrubia, J.J. Boland, Phys. Rev. Lett. **63**, 306 (1989)
30. J.J. Boland, J.S. Villarrubia, Phys. Rev. B. **41**, 9865 (1990)
31. R.D. Schnell, D. Rieger, A. Bogen, F.J. Himpsel, K. Wandelt, W. Steinmann, Phys. Rev. B **32**, 8057 (1985)
32. L.J. Whitman, S.A. Joyce, J.A. Yarmoff, F.R. McFeely, L.J. Terminello, Surf. Sci. **232**, 297 (1990)
33. K. Shudo, H. Washio, M. Tanaka, J. Chem. Phys. **119**, 13077–13082 (2003)
34. M. Tanaka, K. Shudo, M. Numata, Phys. Rev. B **73**, 115326 (2006)
35. J. Iwata, K. Yabana, Kotaibutsuri **39**, 771 (2004). (in Japanese)
36. Zachary H. Levine, Paul Soven, Phys. Rev. A. **29**, 625 (1984)
37. A. Marini, R. Del Sole, A. Rubio, Phys. Rev. Lett. **91**, 256402 (2003)
38. Alessandra Ricca, Charles B. Musgrave, Surf. Sci. **430**, 116 (1999)
39. URL: http://www.gaussian.com/
40. Mark E. Casida, Christine Jamorski, Kim C. Casida, Dennis R. Salahub, J. Chem. Phys. **108**, 4439 (1998)
41. Rüdiger Bauernschmitt, Reinhart Ahlrichs, Chem. Phys. Lett. **256**, 454 (1996)
42. R.E. Stratmann, G.E. Scuseria, J. Chem. Phys. **109**, 8218 (1998)
43. G. Schaftenaar, J.H. Noordik, J. Comput.-Aided Mol. Design, 14, 123–134 (2000) URL: http://www.cmbi.ru.nl/molden/
44. F. Manghi, R. Del Sole, A. Selloni, E. Molinari, Phys. Rev. B. **41**, 9935 (1990)
45. G. Allan, C. Delerue, Phys. Rev. B. **70**, 245321 (2004)
46. M. Murayama, T. Nakayama, Phys. Rev. B. **49**, 5737 (1994)
47. K. Shudo, T. Munakata, Phys. Rev. B. **63**, 125324 (2001)
48. K. Shudo, S. Takeda, T. Munakata, Phys. Rev. B. **65**, 075302 (2002)
49. Handbook of Optical Constants of Solid ed. by E.D. Palik (Academic Press Inc., London, 1985).
50. M. Tanaka, T. Shirao, T. Sasaki, K. Shudo, H. Washio, N. Kaneko, J. Vac. Sci. Technol. A **20**, 1358 (2002)
51. C. Noguez, A.I. Shkrebtii, R. Del Sole, Surf. Sci. **331–333**, 1349 (1995)
52. Y. Owa, K. Shudo, M. Koma, T. Iida, S. Ohno, M. Tanaka, J. Phys.: Condens. Matt. 18, 5895–5903 (2006).
53. P.V. Smith, P.L. Cao, J. Phys.: Condens. Matt. 7, 7125–7139 (1995).
54. R.C. Price, R.L. Whetten, J. Am. Chem. Soc. **2005**, 13750–13751 (2005)
55. H. Kang, T. Park, I. Choi, Y. Lee, E. Ito, M. Hara, J. Noh, Ultramicroscopy **109**, 1011–1014 (2009)
56. K. Shudo, K. Doi, I. Katayama, M. Kitajima, J. Takeda, *Ultrafast Phenomena XVIII, 05013* (EDP Sciences, Les Ulis Cedex, 2012)
57. I. Katayama, S. Koga, K. Shudo, J. Takeda, T. Shimada, A. Kubo, S. Hishita, D. Fujita, M. Kitajima, Nano Lett. **11**, 2648–2654 (2011)
58. M. Shindo, T. Sawada, K. Doi, K. Mukai, K. Shudo, J. of Phys.: Conference Series 441, 012044 (2013).
59. O.V. Misochko, M. Hase, M. Kitajima, Phys. Solid St. **46**, 1741–1749 (2004)

http://www.springer.com/978-3-642-40593-8

Frontiers in Optical Methods
Nano-Characterization and Coherent Control
shudo, k.-i.; Katayama, I.; Ohno, S.-Y. (Eds.)
2014, XII, 228 p. 139 illus., 70 illus. in color., Hardcover
ISBN: 978-3-642-40593-8